Fluid influenced shear wave splitting inversion at Puna, Hawaii

Alan Lucas[1], Kate Lewis Kenedi[1], Eylon Shalev and Peter Malin[1]

[1]University of Auckland, Auckland, New Zealand

a.lucas@auckland.ac.nz

ABSTRACT

Shear wave splitting (SWS) inversion presents a method whereby the upper crust can be interrogated for fracture density. It is caused when a shear wave traverses an area of anisotropy, splits in two, with each wave experiencing a different velocity resulting in an observable separation in arrival times. The current body of work on linear SWS inversion utilises an equation that defines the time delay between arriving shear waves with respect to fracture density. This equation makes the assumption that no fluid flow occurs as a result of the passing shear wave, a situation called squirt flow. This paper shows that the assumption is not applicable in all geological situations. When it is not true, its use in an inversion produces a result which is inaccurate. This is shown to be the case at the test case of 6894 SWS observations gathered in a small area at Puna geothermal field, Hawaii. To rectify this situation, a series of new time delay formulae, applicable to linear inversion, are derived from velocity equations presented in the literature. The new formula uses a `fluid influence parameter' which indicates the degree to which squirt flow is influencing the SWS. It is found that accounting for squirt flow better fits the data and is universally applicable. The fluid influence factor that best describes the data can be identified prior to solving the inversion. Implementing this formula in a linear inversion has a significantly improved fit to the time delay observations than that of the current methods. The Puna data set provides a ground truth support of the techniques through comparison of inversion results to the existing understanding of geological structures provided by drilling results.

1. INTRODUCTION

1.1 Shear wave splitting

Shear wave splitting (SWS) is the measure of seismic velocity anisotropy analogical to birefringence in optics. It presents in earthquake seismographs as two shear wave arrivals usually separated by a small delay in time (0.1s for earthquakes in the upper crust) [CP08]. SWS has several proposed causes, examples of which are: parallel aligned fracture systems [AMC74], lattice preferred orientation [BC91], layered sedimentary fabrics [Bac62].

It is generally found that the velocity variation causing SWS is a small (5-10%) second order effect imposed on top of the much larger magnitude spatial variations in velocity ([Cra84], [Gle91], [CBL91]). However on occasions large (15 to 30%) observations have been made [SPV90]. SWS in the upper crust (the depth range 0 to 5 km) is dominated by fracture based anisotropy. This is due to the pervasive presence and larger effect of fracture anisotropy compared to sedimentary fabrics ([TSB+12], [Cra94], [Kan90], [BC91]). The presence of fractures modifies the potentially isotropic rock matrix so that its stiffness varies depending on the direction of force being applied to it, resulting in different S-wave velocities depending on the direction of polarisation of the S-wave. In this paper, the focus is on the upper crust and thus fracture based anisotropy.

1.2 Theoretical explanations

Almost all theoretical descriptions of SWS follow an effective medium approach [LHP00], [SD88], [CGSP13], [Cha03], [Gur03]). The simplest and most commonly used follow either the isolated (wet or dry) fracture [Hud81] or linked [Tho86] fracture theories.

A fracture system generating a SWS observation occurs at some point along the path of shear wave propagation between earthquake and station. Immediately before entering the area of fracture-based anisotropy the shear wave is linearly polarized in a direction related to the focal mechanism of the earthquake. Upon entering, the wave splits into two approximately orthogonal polarisations due to the velocity anisotropy caused by the fractures (**Figure 1**) [Cra81]. If the initial polarisation is parallel or perpendicular to the orientation of the fractures then no SWS will occur ([Cra81], [Sav99]).

Within a fractured medium, seismic velocity is fastest parallel (V_{para}) to the fractures and slowest perpendicular (V_{perp}) resulting in shear waves polarized parallel (also called the fast wave) and perpendicular to fracture strike (the slow wave) [T+02]. This anisotropy also results in each wave experiencing a different velocity, therefore the more time the waves spend in the fractured area the larger the time delay between the two wave forms. When the waves exit the fracture zone they both experience the same velocity and thus propagate in the same manner but as separate waves.

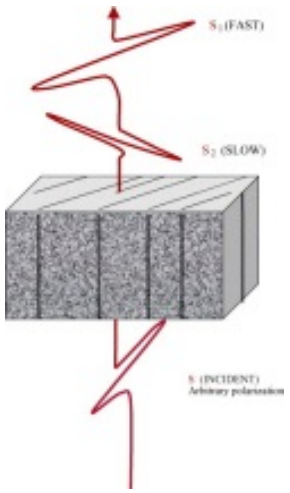

Figure 1: An idealised example of SWS, the randomly polarised S-wave enters the fractured medium at the bottom of the image. The resulting split waves exit at the top with polarisations related to the fracture strike. Image source: [REY05].

1.2.1 Isolated fracture

Crack density is defined as:

$$\epsilon \stackrel{\text{def}}{=} \frac{Na^3}{U} \quad (1)$$

Where ϵ is the crack density and N the number of cracks in a unit volume U. Each crack is defined as a thin, water filled disk with an average radius a. It can be seen that the crack density is a unit-less quantity where un-fractured rock represents a value of $\epsilon = 0$. Using this definition, Hudson [Hud81] derives shear wave velocities parallel and perpendicular (V_{para} and V_{perp}) to the strike of the cracked region. These velocities are then used by Sato [SMN91] to derive a SWS time delay relationship through:

$$\tau = \left(\frac{1}{V_{perp}} - \frac{1}{V_{para}}\right) R \quad (2)$$

Where R is the distance of propagation inside the area of crack density and is the SWS time delay measured at the station. By substitution and making the assumption that $\epsilon \ll 1$, the time delay measured at the station can then be approximated by the first order Taylor series term:

$$\tau = [\cos(4\theta) - \cos(2\theta)]\frac{4\epsilon R}{7\beta} \quad (3)$$

Where τ is the SWS time delay measured at the station and is a function of both the angle of incidence (θ) and crack density (ϵ). The angle of incidence (θ) between the S-wave and fracture plane is defined as the angle between a vector normal to the fracture plane and a vector in the direction of propagation (**Figure 2**). It can be seen that the time delay (τ) has a non-linear relationship with varying incident angle θ as $\tau([\theta_1 + \theta_2], \epsilon) \neq \tau(\theta_1, \epsilon) + \tau(\theta_2, \epsilon)$. Through a similar derivation as used by Sato the SWS time delay for a air filled fracture can be shown to be:

$$\tau = [\tfrac{15}{14} + \tfrac{1}{14}\cos(4\theta) - \tfrac{4}{7} - \tfrac{4}{7}\cos(2\theta)]\frac{\epsilon R}{\beta} \quad (4)$$

Where the variables have the same definitions as for equation 3.

2. LINKED FRACTURE SWS THEORY

The form of linked vertically dipping fractured media velocities as defined by Thomsen [Tho86] and modified Berryman [Ber09] are:

$$V_{para} = \beta\left[1 - \frac{\gamma}{1+2\gamma} sin^2\theta\right] \quad (5)$$

$$V_{para} = \beta\left[1 + \frac{\alpha^2}{\beta^2}(\sigma - \delta) sin^2\theta cos^2\theta\right] \quad (6)$$

where γ, σ and δ are Thomsen's independent anisotropy parameters which typically vary between 0 and 1, (however negative values have been experimentally observed [Tho86]), θ is the angle to the axis of symmetry of the fractures (**Figure 2)**, α and β are the P and S wave velocities and are defined by vertical incidence on the fractured region i.e. along the symmetry axis of the anisotropy and thus no SWS can occur.

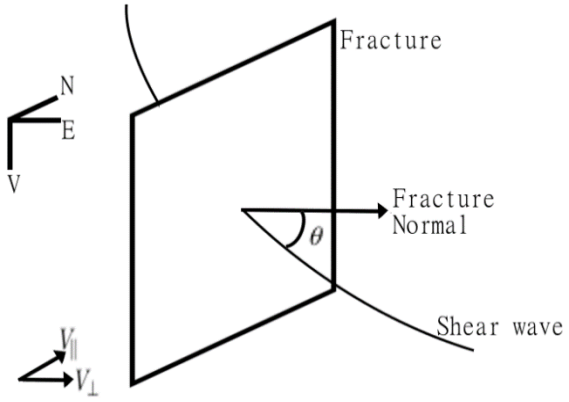

Figure 2: The definition of theta. A fracture system with a north strike and a vertical dip has a corresponding normal vector entirely in the east-west direction. The normal vector lies along the symmetry axes of the anisotropy. Theta is defined as the angle between this normal and the direction of shear wave propagation.

Thomsen's velocities do not as easily apply to analysis the isolated theory. Therefore it is proposed to generate an equivalent time delay formula based on these velocities. If a similar assumption is made (the matrix is a Poisson solid) and that the fluid is an ideal fluid then substitution of Equations 5 and 6 into Equation 2 and following a similar procedure as Sato's derivation of equation (3) results in:

$$\tau = \left[\tfrac{4}{7} - \tfrac{4}{7}\cos(4\theta) + F - F\cos(2\theta)\right]\frac{\epsilon R}{\beta} \quad (7)$$

Where

$$F = \tfrac{3}{8}\left(\tfrac{4}{3} - \tfrac{8}{15}D\right) \quad (8)$$

The use of multiple Taylor series approximations (around $\epsilon = 0$) in this derivation means that Equation 3.8 is only applicable for weak anisotropy. D is called the 'fluid influence factor' and has many possible definitions, most of which are dependent on the unfractured medium's porosity, fluid and medium elastic moduli [Tho95]. It is seen that this formula is algebraically the same as the isolated fracture theory (Equation 3) when:

$$\tfrac{3}{8}\left(\tfrac{4}{3} - \tfrac{8}{15}D\right) \rightarrow -\tfrac{4}{7} \quad (9)$$

and the models are equal when $D = 5\,\frac{5}{14} \sim 5.36$. An equivalent algebraic method is not easily derived with the isolated dry fracture theory. However a graphical inspection (part of wich is displayed in **Figure 3**) allows the conclusion that the dry model is approximately equivalent when $= 3$. This gives some illustration of the realistic range expected for the D parameter, however it does not provide boundaries above or below which the value of D is not physically possible

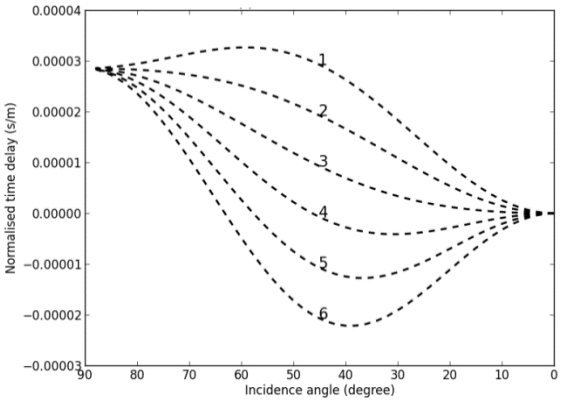

Figure 3: The time delay (normalised by ray length) variation with incidence angle measured from a normal to the vertically dipping fractures (90° is a vertically travelling shear wave) for a range of D values (1 to 6) and with a crack density of $\epsilon = 0.05$.

3. INVERSION THEORY

The generalised inverse problem as implemented in this paper is described as:

$$\boldsymbol{A}(i,j).\boldsymbol{m}(j) = \boldsymbol{o}(i) \qquad 10$$

Where the matrix **A** contains the linear relationship between the model **m** and the observations **o**, and i and j are respectively, the number of observations and model parameters being used in the inversion.

The first step in any SWS inversion is the construction of the forward operator matrix (A). For the methods presented here this requires the identification of which nodes in the model are influencing the SWS observation. It is assumed that SWS anisotropy is entirely caused by fractures and is a small magnitude effect written on top of the bulk shear wave velocity. The ray approximation of the wave equation is applicable, i.e. when the areas of fracturing being investigated are larger than the dominant wavelength of the S-waves. Then the anisotropy causes little deviation from that of a ray propagating through an equivalent isotropic medium. This allows the tracing of all rays from their earthquake sources through a 3D velocity model generated using the method of Shalev and Lees [SL98] to the corresponding station. Tracing is done through the commonly used method of ray bending [UT87] [Nol08].

All of the SWS relationships presented earlier in this paper have a dependence on the angle between the fractures and the shear wave propagation direction. The determination of this angle is critical. These relationships are non-linear due to this directional dependence, and this can be treated through a 'Bayesian' approach by the application of prior information - the incidence angle is determined before the inversion is computed and is not allowed to vary during its computation.

Assuming all fractures have a near-vertical dip, then all that is required is a strike angle and the fracture model is pre-defined. The aim is to determine a normal to the fractures for each node of the inversion model. The method chosen is a three dimensional fracture strike model where the normal are determined for each node separately through a three dimensional version of that proposed by Johnson and Savage [JS12].

For each ray traced (i) and each node (j) in the inversion domain, the velocity, length of ray R inside the node and ray-fracture angle θ are stored in matrices with size i,j, the same as $\boldsymbol{A}$. Any nodes that a ray does not transit are tabulated with a matrix value of zero. As each ray only interrogates a small portion of the inversion domain, these matrices, although potentially large, contain few non-zero elements. Thus they are best constructed and manipulated using sparse matrix techniques. The velocity is interpolated from the model used for the tracing, and the ray length is calculated using basic trigonometry from the entry and exit points of the ray on the node in question.

$$\boldsymbol{A}(i,j) = \left[\frac{4}{7} - \frac{4}{7}\cos\left(4\boldsymbol{\theta}(i,j)\right) + F - F\cos\left(2\boldsymbol{\theta}(i,j)\right)\right]\frac{\boldsymbol{R}(i,j)}{\boldsymbol{\beta}(i,j)}$$

Where F is defined in equation (7) and $\boldsymbol{\theta}(i,j)$, $\boldsymbol{\beta}(i,j)$ and $\boldsymbol{R}(i,j)$ are the matrices of ray-fracture angle, S-wave velocity and ray length inside the node respectively.

As with most geophysical inverse problems the inversion of SWS time delays requires regularisation to reduce the effects of singularities. The methods chosen for this inversion were Laplacian smoothing and/or damping ([LC89], [PVJ93], [TR07]). Laplacian smoothing is implemented by attaching the three-dimensional, finite difference Laplacian operator ($\boldsymbol{L}(i,j)$) to the system and the optimisation of $s.\boldsymbol{L}(i,j).\mathbf{m}(\mathrm{j}) = 0$ (where s is a user-set control on the influence of smoothing). Damping is done in a similar manner though an identity matrix $\mathbf{I}(i,j)$ and the optimisation of $d.\boldsymbol{I}(i,j).\mathbf{m}(\mathrm{j}) = 0$ where d is a user-set control on the influence of damping.

Geophysical inversions are often only approximately linear over small steps in the domain being investigated. To combat this, a perturbation from the starting model is optimised, rather than a direct inversion. If the perturbation is small then to a first order approximation the system is linear, thus the starting model selection has a large influence on the result [SW09].

A linear change with depth model of starting crack densities is constructed by two user-specified values, the crack density at the top and bottom of the model, giving the vector $\boldsymbol{\epsilon}(\mathrm{j})$. It is implemented through first calculating the time delays $\boldsymbol{o_{start}}$ which would result from this model by $\boldsymbol{o_{start}}(j) = \boldsymbol{A}(i,j).\boldsymbol{\epsilon}(\mathrm{j})$ and then removing them from their corresponding observed data.

The total system of equations being solved is:

$$\begin{pmatrix} \boldsymbol{w}\,\boldsymbol{A} \\ s\,\boldsymbol{L} \\ d\,\boldsymbol{I} \end{pmatrix}.\boldsymbol{m} = \begin{pmatrix} \boldsymbol{w}(\boldsymbol{o} - \boldsymbol{o_{start}}) \\ 0 \\ 0 \end{pmatrix} \qquad 12$$

4. INVERSION APPLICATION AT PUNA, HAWAII

The Puna area is located in the Kilauea Volcano Lower East Rift Zone (KLERZ), Hawaii. The rift is locally defined on the surface by a combination of fissure eruption craters and normal faulting, both of which strike NE-SW [MK64]. The KLERZ has been volcanically active in the recent past (last

eruption 1960 [Moo83]) and the resulting lava flows have resurfaced the area, obscuring all fault activity pre-dating the eruption. There is little variation (in the Puna area) from layered basaltic rocks either laterally [MT91] or with depth [MT93], although intrusions and breccias are also present [QGGH00].

In the Puna area the rift makes a left step (looking along rift strike) of approximately 1km with no observed corresponding transverse faulting ([ID85] [MT91]). In the area of the step there is a geothermal system, and the Puna Geothermal Venture Co (PGV) has established a power station. The PGV lease boundary is displayed in **Figure 4**; this is used as a reference point in the figures for this paper. Drilling data provided by PGV indicate that production is concentrated in the southern part of the lease and is fracture controlled [Ken10]. These data also indicate a fault system trending NE and steeply dipping to the NW in the southern section of the lease.

All inversions were calculated in a rectangular domain, with the origin (latitude 19.4583N, longitude 154.9290W) of the local co-ordinate system in the lower left corner of the domain. The dimensions of the domain were chosen as 6km, 7km and 3:5km in the north, east and depth directions respectively (**Figure 4**). The parameterisation of the domain was implemented through dividing it into 147000 cubes with a dimension of 0.1km. For the purposes of displaying inversion results a smaller plotting window is used (**Figure 4**). This represents a cropped section of the total inversion domain used to create the result.

Of the 13581 observations identified during SWS picking a further 4004 were removed as their incidence angle with the surface at the station was greater than 25 degrees from the vertical. This left a final total of 9577 observations, of which 4093 were null and 5484 SWS. Hit plots indicating data coverage will be supplied with all inversion results displayed in this paper. These plots show spatially the number of shear waves which transit each node in the inversion.

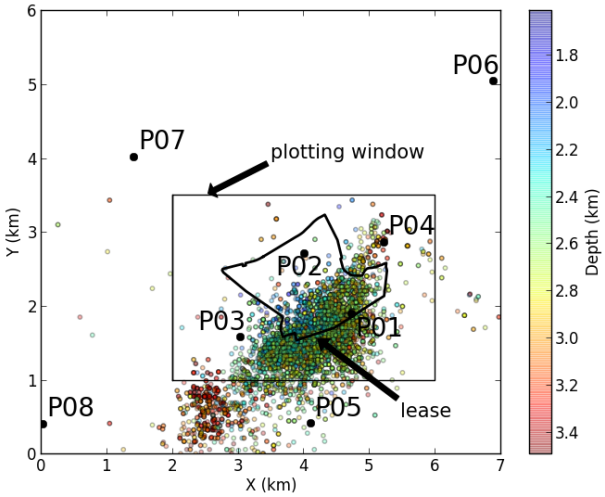

Figure 4: The axes of this figure represent the domain used in all inversions on the Puna data set conducted in this paper. Locations of all earthquakes displaying SWS used to compute inversion results are marked with a circle whose colour indicates the depth. The stations used to gather the seismic data are marked in black circles. The Puna lease boundary, which will be used as a reference point in some results, is marked in a heavy black line. Most results presented will be displayed as a cropped section of the full inversion domain; this plotting window is displayed on here by the box indicated.

4.1 Crack density starting model

A range of homogeneous starting models are investigated through the implementation of:

$$RMS = \sqrt{\frac{\sum_1^i [\boldsymbol{A}(i,j).\boldsymbol{m_s}(j) - \boldsymbol{o}(i)]^2}{N}} \qquad 13$$

Where the model vector $\boldsymbol{m_s}(j)$ is made up of the model being investigated as a potential starting model and N is the number of observations. Two values are used as controls on the model; the crack density at the top and bottom of the inversion domain. The quality of each starting model is identified and a low RMS value represents a high quality model. The application of this relationship to both top and bottom values over a user-set range allows the construction of contour plots (**Figure 5**).

From the point of lowest RMS the optimised model parameters are identified, for the Puna data, linked fracture inversion the values chosen were a top of 0.07 and bottom 0.02. However, it is clear from the plots that there is some degree of ambiguity in the values i.e. the top and bottom pair of 0.08 and 0.00 have a very similar RMS as those chosen.

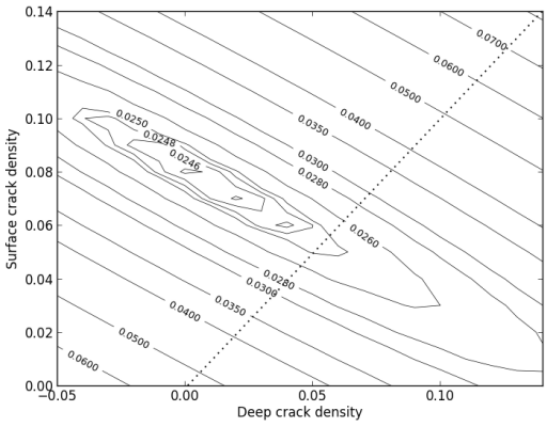

Figure 5: Selection of the linear starting model for an inversion based on the linked fracture theory. The contours are the RMS (in seconds) of the starting model constructed using the y-axis and x-axis crack density values (with a linear change with depth between them) at the respective top and bottom of the inversion domain. The dotted line indicates the range of homogeneous starting models possible and their corresponding RMS.

The contour plots of the linear starting models are directly related to a homogeneous model, i.e. all the cases where the top and bottom values are equal. This can be observed by drawing a diagonal line through these cases in the top plot of **Figure 5**. Above this line the starting model crack density at the surface is larger than that at depth; below, the converse is true. Inversion starting models indicate trends present in the data, e.g. velocity tomography starting models often indicate increasing velocity with depth, a common situation in the earth. Results of the starting model optimisation for Puna linked fracture inversion indicate that

a decreasing crack density with depth fits the data better than increasing crack density. This result is physically sensible as the increasing pressure with depth relationship in the Earth may cause a closing of fractures with depth.

4.2 Fluid influence factor

In linked fracture inversions, the selection of the fluid influence factor (D) presents a challenge for the Puna data set. An optimisation process is used to identify the D that best fits the data. In this optimisation the crack density start model is fixed at the model used in the final inversion calculation. Then for each fluid influence factor start model being evaluated, the forward matrix A is reconstructed based on the parameter and the RMS is calculated by using **equation 13**.

The range of fluid influence factors investigated is from -2 to 8; these values were chosen as they cover the range from the isolated wet to dry theories with some additional freedom. It can be seen that a homogeneous parameter optimises in the region between 1.5 and 2 (Figure 6). In all linked fracture inversions presented in this chapter a value of Dc = 1:75 has been used. This value is not indicative of SWS following a isolated fracture theory.

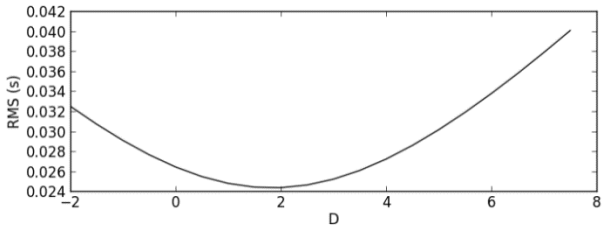

Figure 6: Selection of the fluid influence factor (D). Where the x-axis represents the value of D the model is constructed out of, and the y-axis is the corresponding RMS in seconds of the model. D is unit less.

4.3 Regularisation

Identifying the regularisation parameters which are preferable for inversion of the Puna data set is complex. By setting both of coefficients (smoothing) and (damping) to zero, it is possible to invert without smoothing or damping. This produces an inversion result with low residual but unstable and overprinted with noise from inaccuracies in the picking.

The process whereby the optimum coefficients are selected is a standard 'L curve' approach ([She09], [EP86], [Han92]). Which involves running multiple inversions with changing regularisation and storing the variance both the model and misfit. These are plotted against each other with each point indicating a different regularisation. The curve formed should have an L shape, with the elbow of the L closest to the origin and indicating the preferred value. This works for identifying an optimum smoothing or damping parameter if either is being used alone as regularisation in an inversion. If both are being used the situation becomes more complex due to the interaction between the parameters, i.e. higher and lower damping parameters indicate different optimum smoothing parameters. Although both smoothing and damping are used together in inversions there is no clear technique to be used in their selection ([Zha01], [KHK+00], [SPJT01]).

The method chosen to identify the optimum regularisation parameters for use on the Puna data set was to first fix the Laplacian (s) at zero and use a L curve to identify the optimum damping (d). This was found to be d= 1. Then the damping was fixed at this value and an optimum Laplacian identified. For this the L curve was slightly modified, with the model variance being replaced with a measure of roughness. This was calculated by multiplying the model (m) by the finite difference Laplacian matrix (L) and taking the RMS of the resulting vector.

Roughness was chosen as the standard method of model variance does not indicate the smoothness of a candidate model. The resulting plots are similar to the standard L curve. A Laplacian parameter which is the best trade-off between model smoothness and misfit is desired, this will be at the elbow of the L. The value decided on for use were s= 1.3.

4.4 Inversion results

Crack density inversion based on isolated wet fracture theory with only SWS observations used indicates that coherent anisotropy is present at Puna (Figure 7, left column). At shallow depth (1 to 1.8km) the dominant feature is a crack density high in east of the lease (X = 5km Y = 2km) and a secondary anomaly in the south of the lease (X = 3.5km Y = 1.5km). The ray coverage (Figure 7, right column), however, is low in some areas due to the earthquake and station distribution. At depths of 1km and above rays begin to converge on stations, and at depths of 2:5 km and below rays start to merge due to the distribution of earthquakes. The area of highest confidence in the inversion result is in the south of the lease area.

4.5 Geological Interpretation

Figure 8 shows the geological map of the Puna area, including the PGV lease boundary. A fissure formed in 1955 bisects the lease from southwest to northeast. It is possible that this feature is also the source of the underlying lava flows, dated at 340 years old (Fig. 8) and could therefore possibly be a relatively deep feature or indicative of larger features below. This hypothesis is based on the pattern of the 340 year old flow, seemingly originating at Pu'u Honuau, immediately next to the 1955 fissure and which could be the source of these small cones. The shear wave splitting results (left column of Fig. 7) indicate a high crack density in the east of the lease, southeast of the line of the fissure. We hypothesize that the fissure marks a deep-seated feature that comprises the boundary of the area of high fracture density.

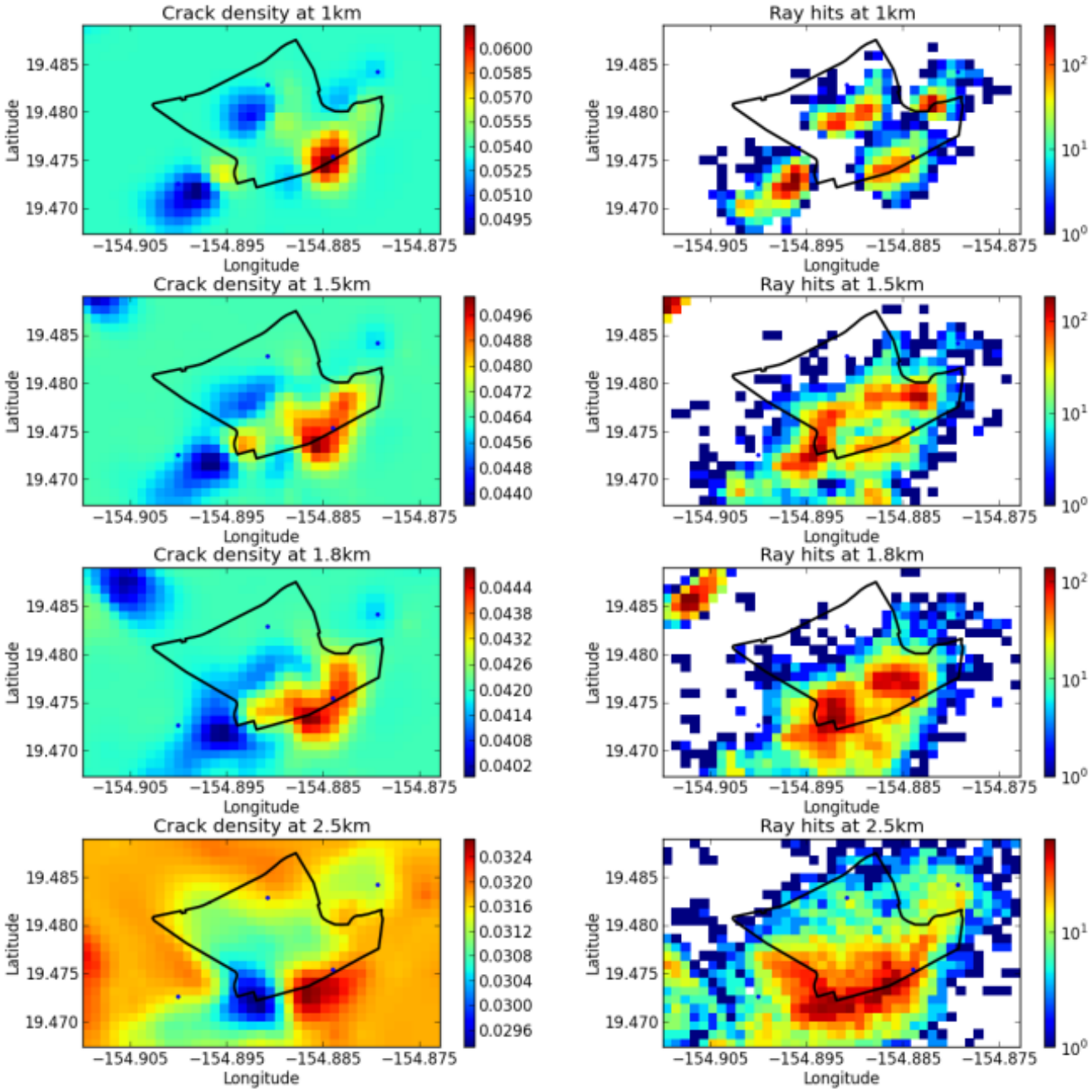

Figure 7: Depth slices of the crack density inversion results for the Puna data set based on the linked fracture model. In the left column are the inversion results and in the right are the corresponding hit plots. The colour scale for the left plots is crack density (a unitless number) and the right is the number of observations which transverse the node (white indicating none). The axes are in the local co-ordinate system. The stations are marked with blue circles and the lease boundary in black. The plot bounds are a cropped section of the total inversion domain.

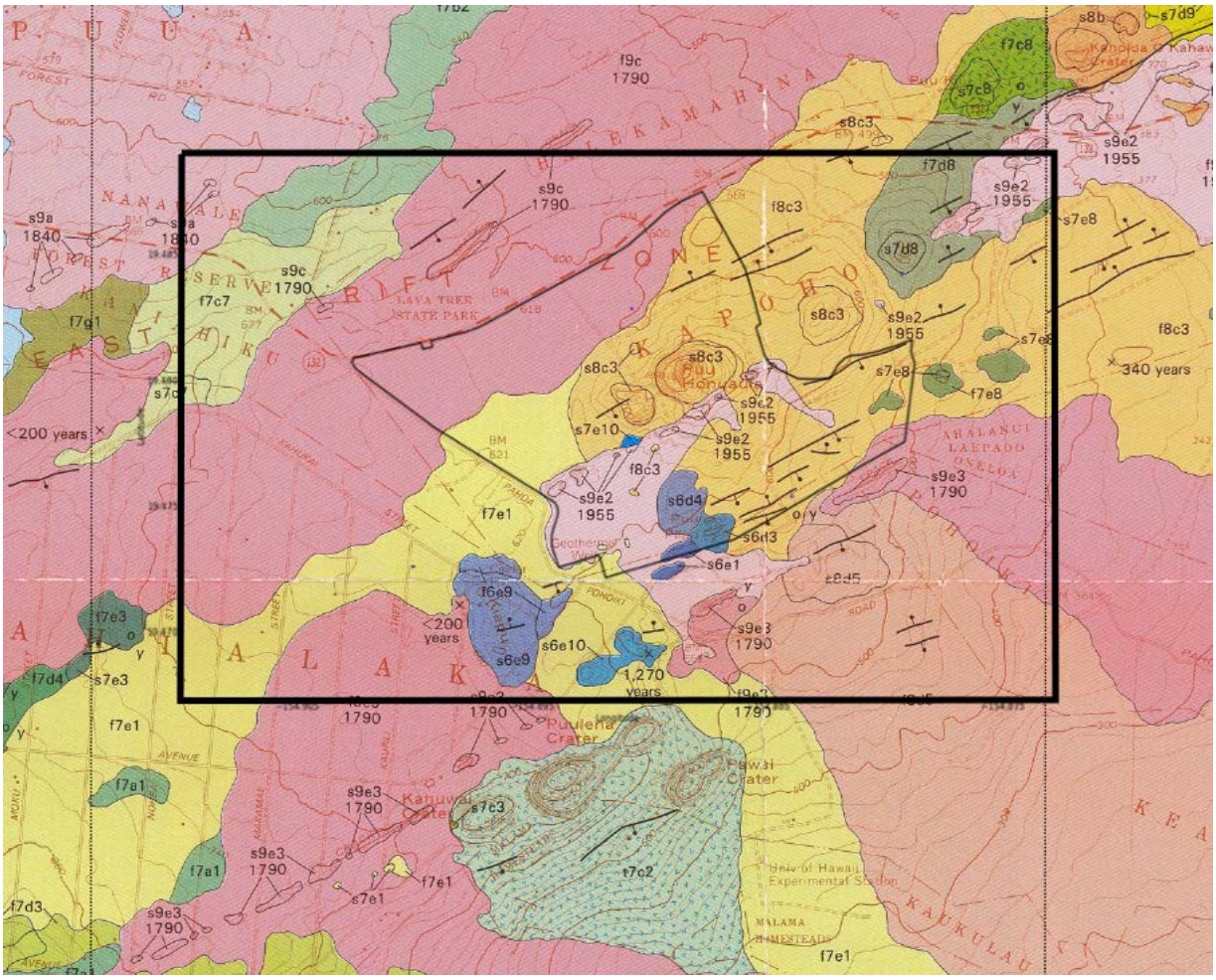

Figure 8 Detail of the Puna surface geology. The background image is a cropped section of Moore and Trusdell [MT91], where the outlines of fissure features are marked with thin black lines and faults are denoted using the standard marking. The geological units are all basic lava flows of differing ages with the age indicated where possible. The overlaid bold black rectangle indicates the boundary of the plotting window used in the display of the Puna inversion results. The overlaid thin black line is the Puna Geothermal Venture lease boundary.

5. CONCLUSIONS

Seismic anisotropy manifested by Shear Wave Splitting (SWS) provides a method of interrogating the upper crust useful for economic/social/environmental reasons. In the upper crust it is assumed that the anisotropy causing SWS is primarily brought about by systems of parallel aligned fractures. Fluids within these influence the SWS observed. This paper significantly improves on the current methods of seismic fracture imaging through shear wave velocity anisotropy inversion.

Past methods of SWS inversion are based on an isolated wet fracture theory ([Hud81] and [SMN91]), which do not take into account fluid flow due to the S-wave fracture interactions producing fluid flow (squirt flow). These methods do not adequately fit all geological situations as is shown in their application to a test data set gathered at Puna Hawaii. It was hypothesised that an improved subsurface fracture imaging result can be achieved through accounting for squirt flow inside the inversion framework. A new formulation to describe SWS time delay with varying crack density was investigated (**Equation 7**). This approach was called the linked fracture theory and accounts for squirt flow with a fluid influence factor [Tho95].

REFERENCES

[AMC74] D.L. Anderson, B. Minster, and D. Cole. *The effect of oriented cracks on seismic velocities. Journal of Geophysical Research*, 79(26):4011–4015, 1974.

[Bac62] G.E. Backus. *Long-wave elastic anisotropy produced by horizontal layering*. Journal of Geophysical Research, 67(11):4427–4440, 1962.

[Ber09] J.G. Berryman. *Aligned vertical fractures, HTI reservoir symmetry and Thomsen seismic anisotropy parameters for polar media*. Geophysical Prospecting, 57(2):193–208, 2009.

[BC91] V. Babuska and M. Cara. *Seismic anisotropy in the Earth*, volume 10. Springer, 1991.

[Cra81] S. Crampin. *A review of wave motion in anisotropic and cracked elastic-media*. Wave Motion, 3(4):343 – 391, 1981.

[Cra84] S. Crampin. *Effective anisotropic elastic constants for wave propagation through cracked solids*. Geophysical Journal International, 76(1):135–145, 1984.

[Cra86] S. Crampin. *Anisotropy and transverse isotropy*. Geophysical Prospecting, 34(1):94–99, 1986.

[Cra94] S. Crampin. *The fracture criticality of crustal rocks*. Geophysical Journal International, 118(2):428–438, 1994.

[Cha03] M. Chapman. *Frequency-dependent anisotropy due to meso-scale fractures in the presence of equant porosity*. Geophysical Prospecting, 51(5):369–379, 2003.

[CBL91] S.P. Cheadle, R.J. Brown, and D.C. Lawton. *Orthorhombic anisotropy: A physical seismic modeling study*. Geophysics, 56(10):1603–1613, 1991.

[CGSP13] J.M. Carcione, B. Gurevich, J.E. Santos, and S. Picotti. *Angular and frequency-dependent wave velocity and attenuation in fractured porous media.* Pure and Applied Geophysics, 170(11):1673–1683, 2013.

[CP08] S. Crampin and S. Peacock. *A review of the current understanding of seismic shear wave splitting in the Earths crust and common fallacies in interpretation.* Wave Motion, 45(6):675 – 722, 2008.

[Gle91] K. R. Gledhill. *Evidence for shallow and pervasive seismic anisotropy in the Wellington Region, New Zealand.* Journal of Geophysical Research: Solid Earth, 96(B13):21503–21516, 1991.

[Hud81] J.A. Hudson. *Wave speeds and attenuation of elastic waves in material containing cracks.* Geophysical Journal of the Royal Astronomical Society, 64(1):133–150, 1981.

[JS12] J.H. Johnson and M.K. Savage. *Tracking volcanic and geothermal activity in the Tongariro Volcanic Centre, New Zealand, with shear wave splitting tomography*. Journal of Volcanology and Geothermal Research, 223224(0):1 – 10, 2012.

[KHK+00] J. Korenaga, W.S. Holbrook, G.M. Kent, P.B. Kelemen, R.S. Detrick, H-C. Larsen, J.R. Hopper, and T. Dahl-Jensen. *Crustal structure of the southeast Greenland margin from joint refraction and reflection seismic tomography*. Journal of Geophysical Research: Solid Earth (1978–2012), 105(B9):21591–21614, 2000.

[Kan90] S. Kaneshima. *Origin of crustal anisotropy: Shear wave splitting studies in Japan.* Journal of Geophysical Research: Solid Earth, 95(B7):11121–11133, 1990.

[LC89] J.M. Lees and R.S. Crosson. *Tomographic inversion for three-dimensional velocity structure at Mount St. Helens using earthquake data*. Journal of Geophysical Research: Solid Earth, 94(B5):5716–5728, 1989.

[LHP00] E. Liu, J.A. Hudson, and T. Pointer. *Equivalent medium representation of fractured rock.* Journal of Geophysical Research: Solid Earth, 105(B2):2981–3000, 2000.

[Nol08] G. Nolet. *A breviary of seismic tomography imaging the interior of the earth and sun*. Cambridge University Press, 2008.

[PVJ93] R.J. Pulliam, D.W. Vasco, and L.R. Johnson. *Tomographic inversions for mantle p wave velocity structure based on the minimization of l2 and l1 norms of International Seismological Centre Travel Time Residuals*. Journal of Geophysical Research: Solid Earth, 98(B1):699–734, 1993.

[Sav04] D. Sava. *Quantitative data integration for fracture characterization using statistical rock physics*. Stanford University Ph.D. thesis, 2004.

[SD88] M. Schoenberg and J. Douma. *Elastic wave propergation in media with parrallel fractures and aligned cracks*. Geophysical Prospecting, 36(6):571–590, 1988.

[SL98] E. Shalev and J.M. Lees. *Cubic B-splines tomography at Loma Prieta*. Bulletin of the Seismological Society of America, 88:256–269, 1998.

[SMN91] M. Sato, N. Matsumoto, and H. Niitsuma. *Evaluation of geothermal reservoir cracks by shear-wave splitting of acoustic emission*. Geothermics, 20(4):197 – 206, 1991.

[SPV90] M.K. Savage,W.A. Peppin, and U.R. Vetter. *Shear wave anisotropy and stress direction in and near Long Valley caldera, California, 1979–1988.* Journal of Geophysical Research: Solid Earth (1978–2012), 95(B7):11165–11177, 1990.

[SW09] S. Stein and M. Wysession. *An introduction to seismology, earthquakes, and earth structure*. John Wiley & Sons, 2009.

[Tho86] L. Thomsen. *Weak elastic anisotropy*. Geophysics, 51(10):1954–1966, 1986.

[Tho95] L. Thomsen. *Elastic anisotropy due to aligned cracks in porous rock.* Geophysical Prospecting, 43(6):805 – 829, 1995.

[T+02] Leon Thomsen et al. *Understanding seismic anisotropy in exploration and exploitation*, volume 5. Society of Exploration Geophysicist, 2002.

[TR07] C Thurber and J Ritsema. *Theory and observations seismic tomography and inverse methods*. Treatise on Geophysics, 1:323–360, 2007.

[TSB+12] P. Tillotson, J. Sothcott, A.I. Best, M. Chapman, and X. Li. *Experimental verification of the fracture density and shear-wave splitting relationship using synthetic silica cemented sandstones with a controlled fracture geometry*. Geophysical Prospecting, 60(3):516–525, 2012.

[UT87] J. Um and C. Thurber. *A fast algorithm for two-point seismic ray tracing.* Bulletin of the Seismological Society of America, 77(3):972–986, 1987.

[Zha01] Dapeng Zhao. *Seismic structure and origin of hotspots and mantle plumes*. Earth and Planetary Science Letters, 192(3):251–265, 2001.